Supporting Information

High-Performance Solution-Processed TIIG-Based Polymer Photodetector with Detectivity Across Scalable SWIR Applications

Rico Holfeuer, Marc Comi, Stefan Schröder, Meriem Bouraoui, Johannes Hofmann, Rik Hooijer, Erkan Aydin, Achim Hartschuh, Mohammed Al-Hashimi, AmirAbbas YousefiAmin, Tayebeh Ameri

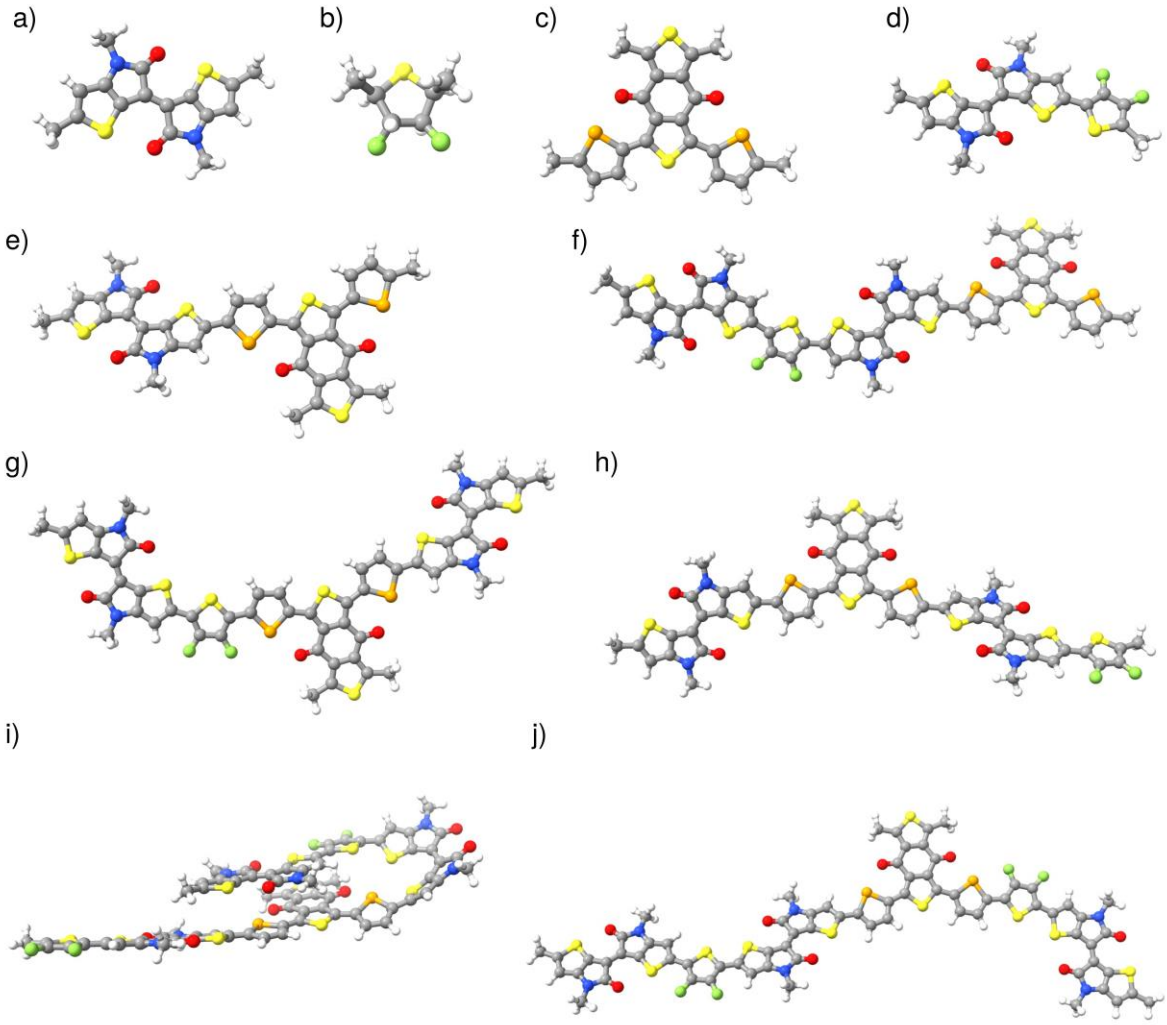

Figure S1: Visualization of optimized structures for **a)** TIIG, **b)** DFT, **c)** DTD-Se, **d)** repeating unit A (= TIIG + DFT), **e)** repeating unit D (= TIIG + DTD-Se), **f)** Dimer A-D, **g)** Dimer A-D*, **h)** Dimer D-A, **i)** Trimer A-D-A and **j)** Trimer A-D-A* (* indicates that the unit is attached in reversed orientation).

Table S1: Key dihedral angles between repeating units (TIIG–DFT, DFT–DTD-Se and TIIG–DTD-Se linkages) extracted from the optimized oligomers (***** indicates that the unit is attached in reversed orientation).

Dihedral Type	*Sequence*	*Dihedral Angle [°]*
TIIG–DFT in A**–**D bond	A**–**D	-8.3
DFT**–**DTD**–**Se in A**–**D* bond	A**–**D*	179.2
TIIG–DTD–Se in D–A bond	D**–**A	157.3
TIIG–DFT in A**–**D bond	A**–**D**–**A	51.8
TIIG–DTD**–**Se in bond D-A	A**–**D**–**A	-167.1
TIIG–DFT in A**–**D bond	A**–**D**–**A*	-6.8
DFT–DTD-Se in D–A* bond	A**–**D**–**A*	-178.7

Table S2: Calculated dihedral angles and relative energies for representative conformers of the A**–**D, A**–**D* and D**–**A dimer describing the TIIG–DFT, DFT–DTD–Se and TIIG–DTD–Se linkage. Relative energies are given with respect to the lowest-energy conformer (***** indicates that the unit is attached in reversed orientation).

Dihedral type	*Syn [°]*	*Anti [°]*	E_{syn} *[E_h]*	E_{anti} *[E_h]*	*ΔE (kcal/mol)*
TIIG**–**DFT in A**–**D	-8.3	-180.0	-10535.087	-10535.087	0.114
DFT–DTD-Se in A–D*	-15.2	179.2	-10535.089	-10535.090	0.560
TIIG–DTD-Se in D–A	-27.1	157.3	-10535.089	-10535.091	0.970

Table S3: Frontier molecular orbital energies (HOMO and LUMO) of the individual molecular segments (TIIG, DFT, and DTD–Se) as well as the full repeating units (A and D), dimer (A–D) and trimer (A–D–A) (***** indicates that the unit is attached in reversed orientation).

	E_{TIIG} *[eV]*	E_{DFT} *[eV]*	$E_{DTD\text{-}Se}$ *[eV]*	E_A *[eV]*	E_D *[eV]*	$E_{A–D}$ *[eV]*	$E_{A–D–A}$ *[eV]*	$E_{A–D–A^*}$ [eV]
LUMO	-0.6364	2.9024	-0.3269	-0.9144	-0.9781	-1.1297	-1.3783	-1.3544
HOMO	-7.1920	-9.1047	-7.5752	-7.1604	-7.0142	-7.0012	-7.0054	-6.9154
ΔE	6.5556	12.0071	7.2483	6.2460	6.0361	5.8823	5.6271	5.5996

Figure S2:

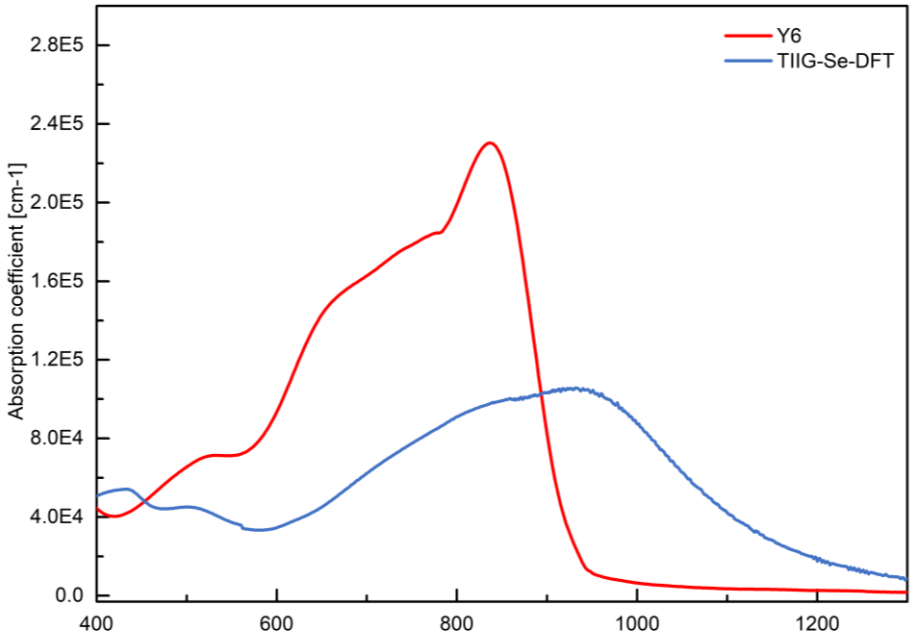

Figure S2: Illustration of the absorption coefficient of the single component thin films, demonstrating an absorption coefficient of 2.3 × 10^5 cm^{-1} and 1.1 × 10^5 cm^{-1} for Y6 and TIIG-Se-DFT, respectively.

Figure S3:

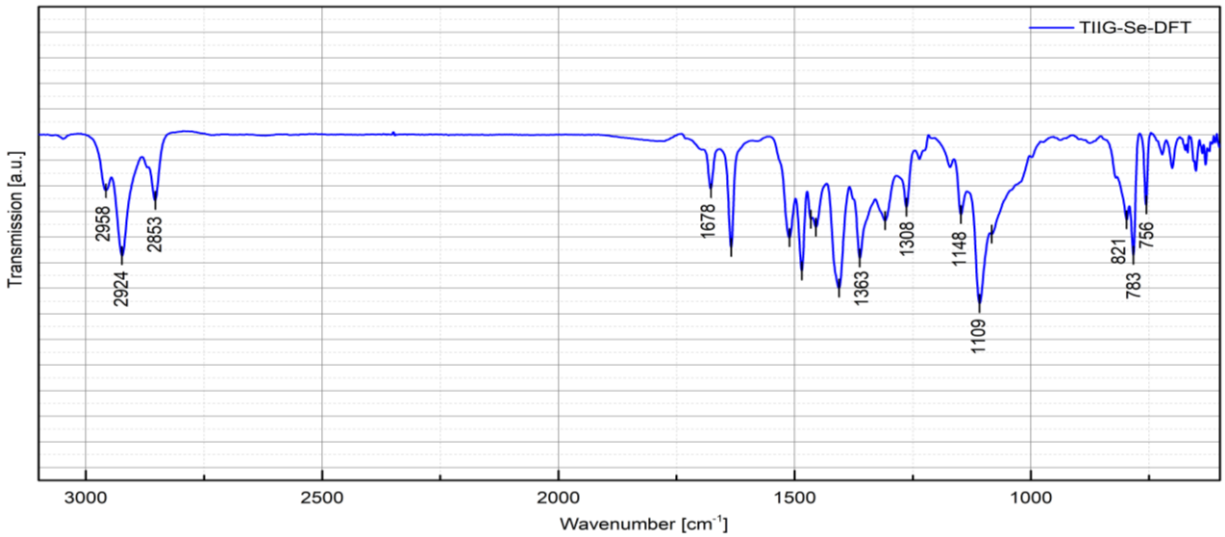

Figure S3: Fourier-transform infrared (FTIR) spectrum of TIIG-Se-DFT:

Aliphatic C-H stretches from side chains at 2958, 2924, and 2853 cm^{-1}; a prominent C=O (lactam) stretch of the TIIG core at 1678 cm^{-1}; aromatic C=C features around 1515-1450 cm^{-1}; TIIG backbone C-N stretches at 1363 and 1308 cm^{-1}; ring C-S-C vibrations as a shoulder/multiplet in the 1260-1210 cm^{-1} region; and distinct C-F stretches from the difluorothiophene units at 1148 and 1109 cm^{-1}. Out-of-plane aromatic C-H bending modes of the TIIG/thiophene rings appear at 821, 783, and 756 cm^{-1} (with weaker bands near 730-680 cm^{-1}), collectively confirming incorporation of the designed structural motifs.

Table S4: Device Architectures & Process Complexity Overview in State-of-the-Art OPDs: Solution vs. Vacuum Deposition

Device Architecture	*Solution-Processed Layers*	*Vapor Deposited Layers*	*Device Type*	*Process-Complexity Level*	*Spectral Response (nm)*	*Year*
TIIG-Se-DFT:Y6/Au (this work)	1	1	MSM-IDE	■□□	350-1600	2025
ITO/ZnO/PTB7-Th:BTQ-1/MoO3/Al[1]	2	3	vert. Stack	■■□	500-1400	2025
ITO/ZnO/PDPPDTP:TPCTO-2F/MoO3/Au[2]	2	3	vert. Stack	■■□	300-1400	2025
ITO/ZnO/PDPPTBBT:Y6/MoO3/Au[3]	2	3	vert. Stack	■■□	500-1200	2025
ITO/ZnO/PFN-Br/PDPPTDTPT:P4TOC-DCBT/MoO3/Ag[4]	3	3	vert. Stack	■■■	400-1300	2025
ITO/PEDOT: PSS/PTQHT :BTP-4Cl/C60/Au[5]	2	3	vert. Stack	■■□	400-1600	2025
ITO/ZnO/PTB7-Th:Y-QC4F/MoO3/Au[6]	2	3	vert. Stack	■■□	400-1600	2024
ITO/ZnO/PBDT-TT:TBzICF/MoO3/Au[7]	2	3	vert. Stack	■■□	400-1400	2024
ITO/ZnO/PTB7-Th:TTD(DTC-2FIC)2/MoO3/Ag[8]	2	3	vert. Stack	■■□	400-1400	2024
ITO/ZnO/PCE10:BDP4Cl/MoO3/Au[9]	2	3	vert. Stack	■■□	400-1200	2024
H-ITO/CuSCN/PTB7-Th:ATT-X-Fin/PDINN/Au[10]	3	2	vert. Stack	■■□	400-1300	2024
ITO/PEDOT:PSS/PCE10:FB-C6/PDINO/Al[11]	3	2	vert. Stack	■■□	350-1150	2024
ITO/ZnO/PCE10:TPA-4F/MoO3/Ag[12]	2	3	vert. Stack	■■□	400-1200	2024
ITO/ZnO/PBDT-TT:DPPSe-4Cl:Y6/MoO3/Ag[13]	2	3	vert. Stack	■■□	300-1100	2024
ITO/PEDOT: PSS/CDT-TQ:PC71BM/ZnO/Al[14]	3	2	vert. Stack	■■□	600-1400	2024
ITO/ZnO/PTB7-Th:L2:Y6/MoO3/Ag[15]	2	3	vert. Stack	■■□	400-1250	2023
ITO/ZnO/PBDB:OTB4/MoO3/Ag[16]	2	3	vert. Stack	■■□	400-1280	2023
ITO/ZnO/TQ-T:IEICO-4F /MoO3/Ag[17]	2	3	vert. Stack	■■□	400-1500	2023
ITO/ZnO/PTB7-Th:COTCN2/MoO3/Ag[18]	2	3	vert. Stack	■■□	350-1200	2022
ITO/ZnO/TQ-T:IEICO-4F /MoO3/Ag[19]	2	3	vert. Stack	■■□	400-1800	2022
ITO/C60/TQ-P1: Y7 /PEDOT:PSS/Ag-ITO[20]	2	4	vert. Stack	■■■	400-1500	2022
ITO/PFNBr/IFTPA/PCE10:COTIC-4Clr:PCBM71/MoO3/Al[21]	3	3	vert. Stack	■■■	300-1200	2021
Au/ZnO/PCDTPTSe:PC71BM /MoO3/Ag[22]	2	3	vert. Stack	■■□	400-1500	2021
ITO/ZnO/PEIE/PTTQn:PC71BM/MoO3/Ag[23]	3	3	vert. Stack	■■■	400-1600	2021
ITO/ZnO/donor:PC71BM/MoO3/Al[24]	2	3	vert. Stack	■■□	600-1400	2020
Ag/D6:C60/MoO3/Au/Ag[25]	0	5	vert. Stack	■■■	400-1600	2020
ITO/ZnO/DPP-DTT:IR-Dye/MoO3/Ag[26]	2	3	vert. Stack	■■□	400-1600	2020
ITO/ZnO/PTTQ(BO):PC71BM/MoO3/Ag[27]	2	3	vert. Stack	■■□	400-1500	2020
ITO/PEDOT:PSS/C=CPhCDT-co-PSe: PC61BM/ZnO/Al[28]	3	2	vert. Stack	■■□	300-1300	2019
ITO/PEDOT:PSS/P1-CA:PC70BM/ZnO/Al[29]	3	2	vert. Stack	■■□	600-1400	2018
ITO/ZnO/CPDT-TQ:PCBM /MoO3/Ag[30]	2	3	vert. Stack	■■□	300-1550	2018
ITO/PEDOT:PSS/P1:PC61BM/BCP/Al[31]	2	3	vert. Stack	■■□	300-1600	2018
ITO/AZO:PDNI/P1:PC61BM/BCP/Al[32]	2	3	vert. Stack	■■□	300-1540	2018
ITO/Ppy/PBBTPD: Tri-PC61BM/Ba/Al[33]	2	3	vert. Stack	■■□	350-2500	2018

Table S4: Device Architectures & Process Complexity Overview in State-of-the-Art OPDs: Solution vs. Vacuum Deposition						
Device Architecture	***Solution-Processed Layers***	***Vapor Deposited Layers***	***Device Type***	***Process-Complexity Level***	***Spectral Response (nm)***	***Year***
ITO/AZO:PDIN/DPP-TQ-CA:PC70BM/BCP/Al[32]	2	3	vert. Stack		400-1600	2018
ITO/PEIE:ZnO/CPDT-TQ:PC71BM/MoO3/Ag[30]	2	3	vert. Stack		600-1550	2018
ITO/PEDOT:PSS/PDT:PC61BM/BCP/Al[34]	2	3	vert. Stack		300-1600	2017
ITO/PEIE/AP5: PC71BM/MoO3/Ag[35]	2	3	vert. Stack		600-1800	2017
ITO/MoO3/1-TPFB-Salt/C60 /BCP/Ag[36]	1	5	vert. Stack		400-1500	2016
ITO/PEDOT:PSS/P1:PC61BM/BCP/Al[37]	2	3	vert. Stack		300-1200	2015

Single solution layer + 1 metal

5 total layers: multiple solution + multiple vacuum steps

> 5 total layers with min. 3 vacuum steps or full-vacuum stack

Figure S4:

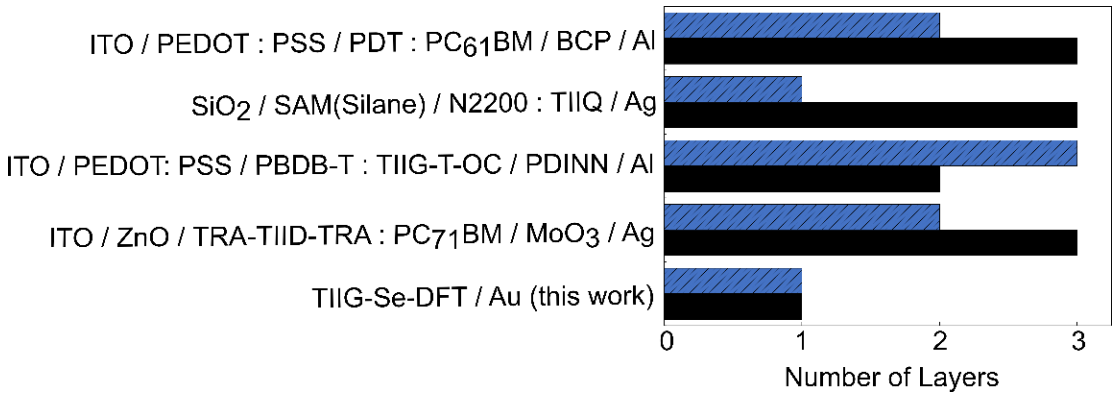

Figure S4: Detailed illustration of the device architecture of the best TIIG-based NIR-SWIR OPDs benchmarked against the sum of vacuum- (black) vs. solution (blue) deposited layers. This demonstrates low fabrication complexity of our single film MSM-IDE device – beneficial for large-scale manufacturing.

Figure S5:

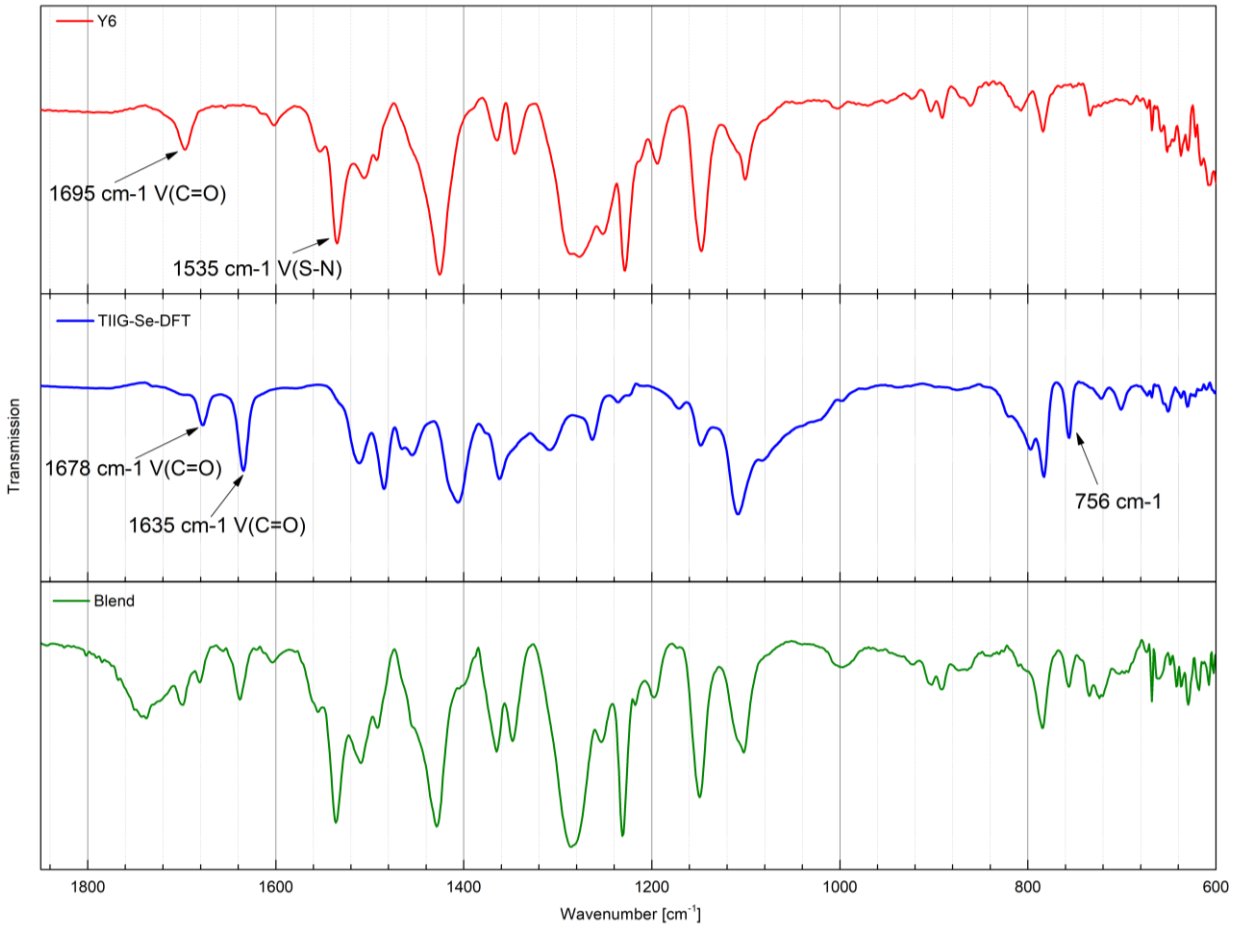

Figure S5: FTIR transmission spectra of Y6 (top, red), TIIG-Se-DFT (middle, blue), and their blend (bottom, green). Characteristic vibrational modes are labelled, including the C=O stretching at 1695 cm^{-1} and the C=N stretching at 1535 cm^{-1} in Y6, and a distinct band at 756 cm^{-1} in TIIG-Se-DFT. The blend spectrum shows features from both components, indicating molecular interactions and preservation of key functional groups.

Figure S6:

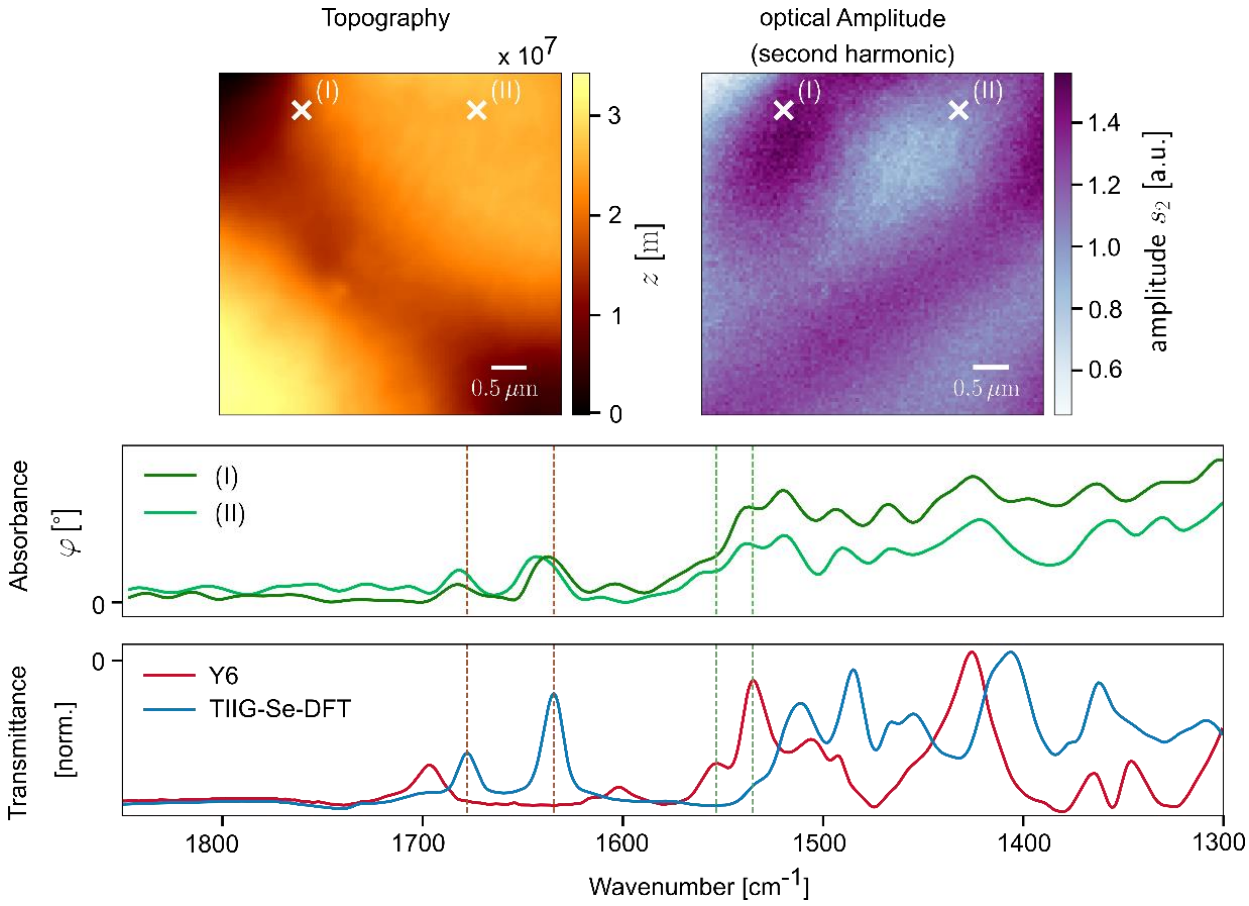

Figure S6: A NanoFTIR-AFM study was performed to investigate both morphology and composition of the films. Upper panels present the topography (left) and optical phase (right) images of the donor-rich TIIG-Se-DFT:Y6 film, along with near-field NanoFTIR spectra obtained at two distinct points [region (I), dark green; region (II), bright green]. The spectra confirm a homogeneous blend. The lower panel highlights the far-field FTIR measurements for the single-component films [TIIG-Se-DFT (blue) and Y6 (red)], revealing that both materials, TIIG-Se-DFT (1643 cm^{-1}) and Y6 (1681 cm^{-1}) are successfully incorporated into the BHJ blend.

Figure S7:

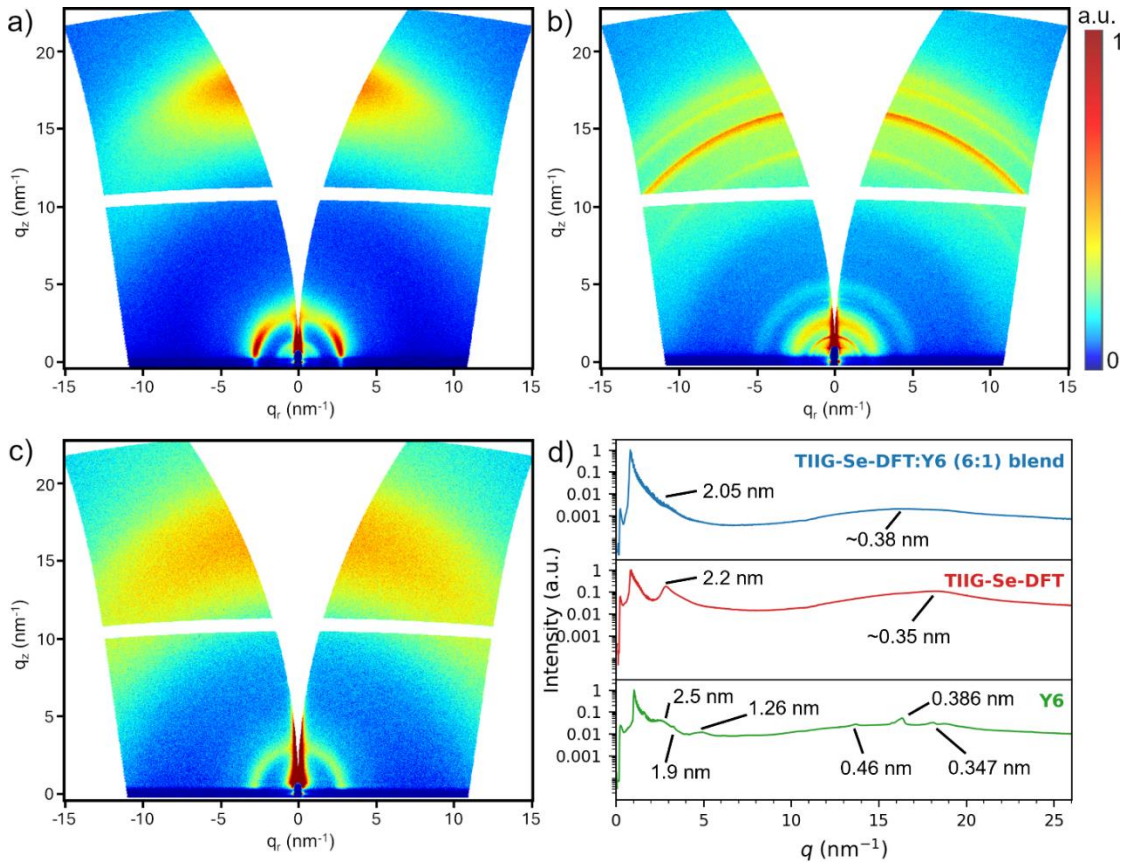

Figure S7: 2D GIWAXS images of (**a**) neat TIIG-Se-DFT donor polymer, (**b**) neat Y6 acceptor, and (**c**) donor-rich TIIG-Se-DFT:Y6 blend (6:1). (d) Pie cut integrated intensity profiles over the full 2D detector images in (a)-(c), with corresponding real-space spacings ($d = 2\pi/q$) indicated for the main reflections.

For neat TIIG-Se-DFT (a), the broad reflection at $d \approx 0.35$ nm appears along q_z (out-of-plane) and is assigned to π-π stacking, while the reflection at $d \approx 2.2$ nm appears along q_r and corresponds to lamellar side-chain stacking. This indicates a predominant face-on orientation of TIIG-Se-DFT with respect to the substrate.

Neat Y6 (b) shows several reflections distributed largely isotropically in reciprocal space, indicating polycrystalline ordering without a strongly preferred orientation. It features three distinct π-π stacking distances at 0.46 nm, 0.386 nm, and 0.347 nm, covering the broad π-π stacking range of Y6. The reflection at d ≈ 0.347 nm can be assigned to the (010) plane of Y6. The low-*q* reflections at $d \approx 1.26$ nm, 1.9 nm, and 2.5 nm reflect longer-range Y6 packing motifs, including end-group and lamellar type ordering.[38]

The TIIG-Se-DFT:Y6 (6:1) blend (c) resembles the neat TIIG-Se-DFT pattern, with a broad π-π stacking reflection around d ≈ 0.38 nm and a low-*q* reflection, slightly smaller than for neat TIIG-Se-DFT (2.2 nm) at 2.05 nm, consistent with intermixing of Y6 into the donor lattice. Both reflections are mostly isotropic, indicating a slight face-on orientation. No specific Y6 reflections are visible, pointing to a well-intermixed, weakly-textured bulk-heterojunction.

Figure S8:

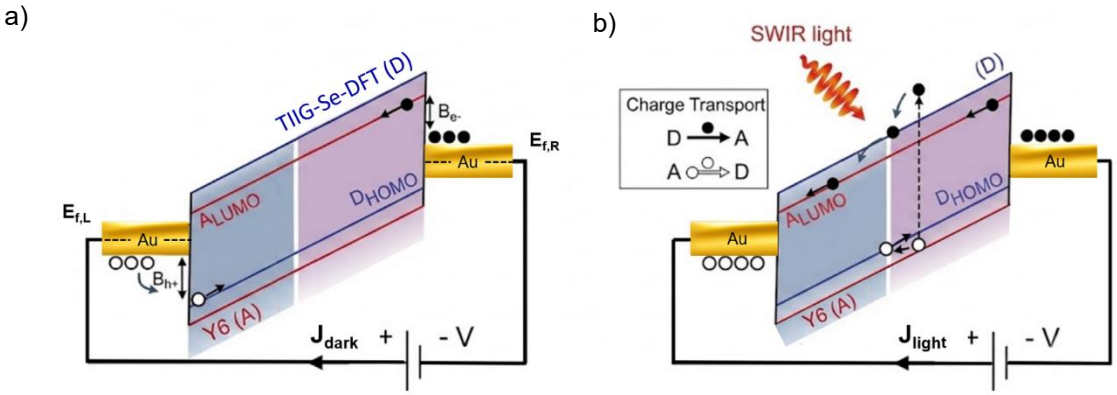

Figure S8: Qualitative schematic illustration of the operating principle and effective energy-level alignment of the lateral Au/TIIG-Se-DFT:Y6/Au MSM photodetector under applied bias. (**a**) In the dark, the Au electrodes form back-to-back Schottky contacts with the TIIG-Se-DFT:Y6 bulk heterojunction, and the current is governed by contact-limited injection, resulting in low dark current. (**b**) Under SWIR illumination, excitons generated in the active layer dissociate at donor–acceptor interfaces, and the resulting carriers are separated and transported laterally by the applied electric field, consistent with field-assisted photoconductive MSM operation. Here, $E_{f,L}$ and $E_{f,R}$ denote the left and right Au Fermi levels under applied bias, B_{h+} and B_{e-} denote the hole and electron injection barriers, respectively, and J_{dark} and J_{light} correspond to the dark current and photocurrent.

Figure S9:

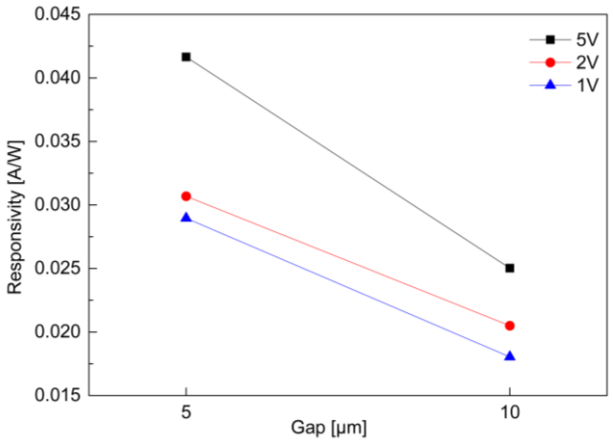

Figure S9: Responsivity as a function of the electrode gap in MSM-IDE photodetectors: Devices with gap sizes of 5 μm and 10 μm showed increasing responsivity with decreasing gap width and increasing applied bias. The trend is consistent with stronger lateral electric fields, shorter carrier transit lengths, and increased effective electrode interface at smaller gaps, supporting field-assisted photoconductive MSM operation.

Figure S10:

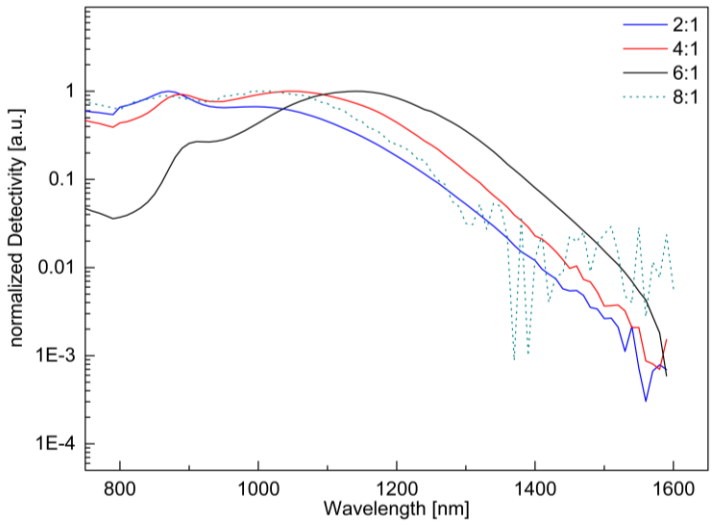

Figure S10: Effect of (D)-(A) composition on broadband detectivity of TIIG-Se-DFT:Y6 OPDs.
Normalized specific detectivity (*D**) spectra measured at 1 V for devices with a D : A weight ratio of 2 : 1 (blue), 4 : 1 (red), 6:1 (black) and 8 : 1 (dotted), covering 400-1600 nm.
Telecom-band advantage: At the eye-safe 1550 nm line the 6 : 1 device delivers a D* ≈ 3 × higher than the 4 : 1 blend and ≈ 9 × higher than 2 : 1, reflecting the greater SWIR photon harvesting of the ultralow-band-gap donor while the Y6 network still ensures efficient electron extraction.
Migration of the Y6 shoulder: The small feature near 900 nm, originating from the Y6 Q-band, red-shifts (≈ 15 nm) and decreases in amplitude as the acceptor fraction is decreased. This behavior is consistent with dilution of pure-Y6 domains and stronger (D)-(A) electronic coupling.
Global envelope shift: Because TIIG-Se-DFT dominates absorption beyond ≈ 950 nm, increasing its volume fraction causes the overall detectivity envelope to extend further into the SWIR.
"Sweet-spot" composition: A 6 : 1 blend maximizes SWIR absorption without disrupting charge-transport pathways, yielding the highest on/off ratio and the smoothest D* trace. At 8 : 1, the Y6 content becomes too low to form an efficient (D)-(A) blend. This is likely to weaken the continuity of the acceptor network, resulting in a noisier and less smooth detectivity spectrum, and causing the spectral envelope to no longer follow the redshift trend observed between 2 : 1 and 6 : 1. We therefore interpret 8 : 1 as the onset of morphology-limited behavior caused by excessive donor enrichment. These trends show that 6 : 1 is the optimum composition, combining broadband light harvesting with low recombination losses to produce the best overall NIR-SWIR detectivity in this MSM architecture.

Figure S11:

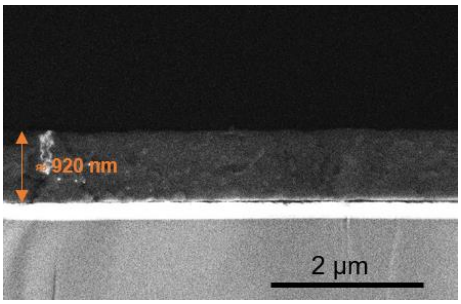

Figure S11: Cross-sectional SEM image of the MSM-IDE single-active-layer photodetector, showing an active-layer thickness of approximately 920 nm for the TIIG-Se-DFT:Y6 blend.

Figure S12:

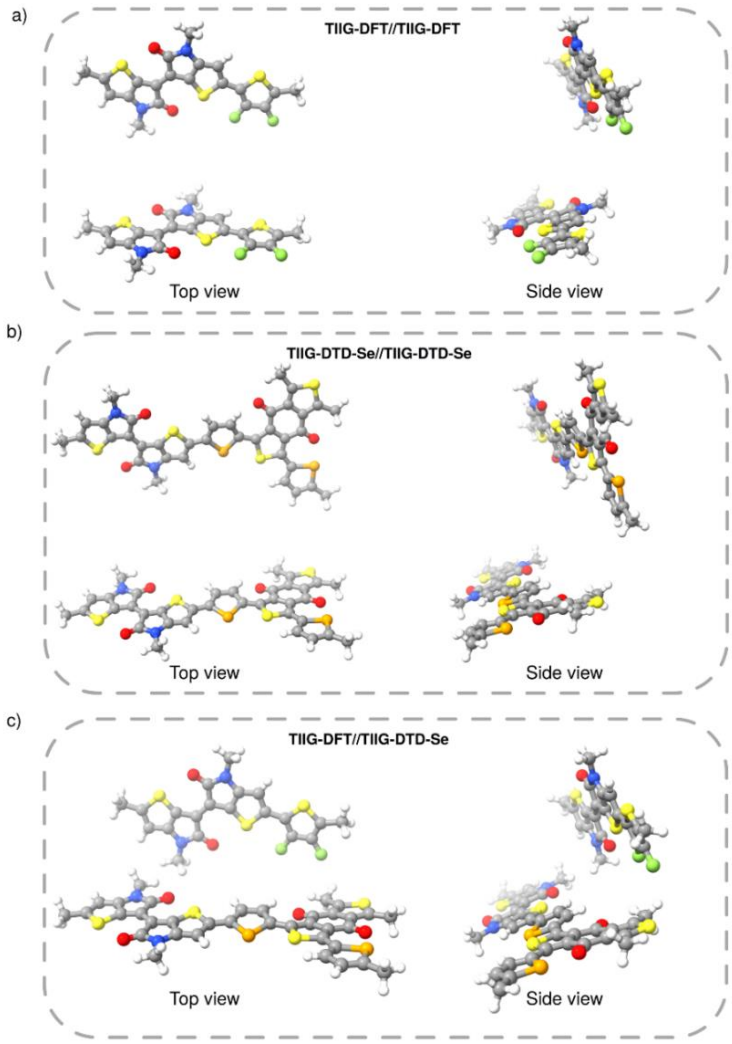

Figure S12: Visualization of the initial molecular positions for the interaction analysis.

Literature

[1] T. Yuan, W. Chen, J. Miao, J. Liu, *Journal of Materials Chemistry C* **2025**, 13, 8623.

[2] H. Hou, W. Wang, T. Li, Z. Zhang, X. Miao, G. Cai, X. Lu, Y. Yi, Y. Lin, *Angew Chem Int Ed Engl* **2025**, 64, e202425420.

[3] M. K. Jeong, S. H. Lee, Y. Won, J. Ahn, M. I. Kim, J. H. Oh, *ACS Appl Mater Interfaces* **2025**, 17, 25591.

[4] X. Chen, Y. Zhu, Y. Xu, M. Rao, P. Pang, B. Zhang, C. Xu, W. Ni, G. Li, J. Wu, M. Li, Y. Chen, Y. Geng, *Angew Chem Int Ed Engl* **2025**, 64, e202413965.

[5] Z. Hu, M. Fu, J. Chen, J. Xie, Y. Dou, H. Li, S. Liu, L. Shao, H. Cai, Y. Zhang, W. Wang, S. Dong, X. Yang, C. Liu, F. Huang, Y. Cao, *ACS Appl Mater Interfaces* **2025**, 17, 28447.

[6] Y. Zhang, J. Chen, J. Yang, M. Fu, Y. Cao, M. Dong, J. Yu, S. Dong, X. Yang, L. Shao, Z. Hu, H. Cai, C. Liu, F. Huang, *Adv Mater* **2024**, 36, e2406950.

[7] B. Yin, X. Zhou, Y. Li, G. Hu, W. Wei, M. Yang, S. Jeong, W. Deng, B. Wu, Y. Cao, B. Huang, L. Pan, X. Yang, Z. Fu, Y. Fang, L. Shen, C. Yang, H. Wu, L. Lan, F. Huang, Y. Cao, C. Duan, *Adv Mater* **2024**, 36, e2310811.

[8] H. Zhang, R. Mao, L. Yuan, Y. Wang, W. Liu, J. Wang, H. Tai, Y. Jiang, *ACS Appl Mater Interfaces* **2024**, 16, 9088.

[9] M. Yang, B. Yin, G. Hu, Y. Cao, S. Lu, Y. Chen, Y. He, X. Yang, B. Huang, J. Li, B. Wu, S. Pang, L. Shen, Y. Liang, H. Wu, L. Lan, G. Yu, F. Huang, Y. Cao, C. Duan, *Chem* **2024**, 10, 1425.

[10] Y. Chen, Y. Zheng, J. Wang, X. Zhao, G. Liu, Y. Lin, Y. Yang, L. Wang, Z. Tang, Y. Wang, Y. Fang, W. Zhang, X. Zhu, *Sci Adv* **2024**, 10, eadm9631.

[11] Y. Wang, J. Wang, J. Miao, J. Liu, L. Wang, *CCS Chemistry* **2024**, 6, 2794.

[12] L. Shao, J. Yang, Y. Huang, Y. Cao, J. Jing, X. Qin, X. Yang, H. Tang, C. Liu, F. Huang, Y. Cao, *Chemistry of Materials* **2024**, 36, 5775.

[13] Y. Wang, M. Yang, B. Yin, B. Wu, G. Liu, S. Jeong, Y. Zhang, C. Yang, Z. He, F. Huang, Y. Cao, C. Duan, *ACS Appl Mater Interfaces* **2024**, 16, 66846.

[14] T. Bills, C. T. Liu, J. Lim, N. Eedugurala, P. Mahalingavelar, B. Seo, E. T. Hanna, T. N. Ng, J. D. Azoulay, *Advanced Functional Materials* **2024**, 34.

[15] T. Li, G. Hu, L. Tao, J. Jiang, J. Xin, Y. Li, W. Ma, L. Shen, Y. Fang, Y. Lin, *Sci Adv* **2023**, 9, eadf6152.

[16] J. Xu, Y. Zhang, J. Liu, L. Wang, *Angewandte Chemie* **2023**, 135.

[17] P. Jacoutot, A. D. Scaccabarozzi, D. Nodari, J. Panidi, Z. Qiao, A. Schiza, A. D. Nega, A. Dimitrakopoulou-Strauss, V. G. Gregoriou, M. Heeney, C. L. Chochos, A. A. Bakulin, N. Gasparini, *Sci Adv* **2023**, 9, eadh2694.

[18] J. W. Ha, H. J. Eun, B. Park, H. Ahn, D. R. Hwang, Y. S. Shim, J. Heo, C. Lee, S. C. Yoon, J. H. Kim, S. J. Ko, *Advanced Functional Materials* **2022**, 33.

[19] P. Jacoutot, A. D. Scaccabarozzi, T. Zhang, Z. Qiao, F. Anies, M. Neophytou, H. Bristow, R. Kumar, M. Moser, A. D. Nega, A. Schiza, A. Dimitrakopoulou-Strauss, V. G. Gregoriou, T. D. Anthopoulos, M. Heeney, I. McCulloch, A. A. Bakulin, C. L. Chochos, N. Gasparini, *Small* **2022**, 18, e2200580.

[20] I. Park, C. Kim, R. Kim, N. Li, J. Lee, O. K. Kwon, B. Choi, T. N. Ng, D. S. Leem, *Advanced Optical Materials* **2022**, 10.

[21] Z. Zhong, F. Peng, L. Ying, G. Yu, F. Huang, Y. Cao, *Science China Materials* **2021**, 64, 2430.

[22] J. Yang, J. Huang, R. Li, H. Li, B. Sun, Q. Lin, M. Wang, Z. Ma, K. Vandewal, Z. Tang, *Chemistry of Materials* **2021**, 33, 5147.

[23] S. Gielen, C. Kaiser, F. Verstraeten, J. Kublitski, J. Benduhn, D. Spoltore, P. Verstappen, W. Maes, P. Meredith, A. Armin, K. Vandewal, *Adv Mater* **2020**, 32, e2003818.

[24] N. Li, J. Lim, J. D. Azoulay, T. N. Ng, *Journal of Materials Chemistry C* **2020**, 8, 15142.

[25] Y. Wang, B. Siegmund, Z. Tang, Z. Ma, J. Kublitski, S. Xing, V. C. Nikolis, S. Ullbrich, Y. Li, J. Benduhn, D. Spoltore, K. Vandewal, K. Leo, *Advanced Optical Materials* **2020**, 9.

[26] N. Li, Z. Lan, Y. S. Lau, J. Xie, D. Zhao, F. Zhu, *Adv Sci (Weinh)* **2020**, 7, 2000444.

[27] F. Verstraeten, S. Gielen, P. Verstappen, J. Raymakers, H. Penxten, L. Lutsen, K. Vandewal, W. Maes, *Journal of Materials Chemistry C* **2020**, 8, 10098.

[28] W. Yao, Z. Wu, E. Huang, L. Huang, A. E. London, Z. Liu, J. D. Azoulay, T. N. Ng, *ACS Applied Electronic Materials* **2019**, 1, 660.

[29] Z. Wu, Y. Zhai, W. Yao, N. Eedugurala, S. Zhang, L. Huang, X. Gu, J. D. Azoulay, T. N. Ng, *Advanced Functional Materials* **2018**, 28.

[30] Z. Wu, W. Yao, A. E. London, J. D. Azoulay, T. N. Ng, *Advanced Functional Materials* **2018**, 28.

[31] J. Han, D. Yang, L. Hu, D. Ma, W. Qiao, Z. Y. Wang, *ChemistrySelect* **2018**, 3, 7385.

[32] J. Han, D. Yang, D. Ma, W. Qiao, Z. Y. Wang, *Advanced Optical Materials* **2018**, 6.

[33] L. Zheng, T. Zhu, W. Xu, L. Liu, J. Zheng, X. Gong, F. Wudl, *Journal of Materials Chemistry C* **2018**, 6, 3634.

[34] J. Han, J. Qi, X. Zheng, Y. Wang, L. Hu, C. Guo, Y. Wang, Y. Li, D. Ma, W. Qiao, Z. Y. Wang, *Journal of Materials Chemistry C* **2017**, 5, 159.

[35] A. E. London, L. Huang, B. A. Zhang, M. B. Oviedo, J. Tropp, W. Yao, Z. Wu, B. M. Wong, T. N. Ng, J. D. Azoulay, *Polymer Chemistry* **2017**, 8, 2922.

[36] M. Young, J. Suddard-Bangsund, T. J. Patrick, N. Pajares, C. J. Traverse, M. C. Barr, S. Y. Lunt, R. R. Lunt, *Advanced Optical Materials* **2016**, 4, 1028.

[37] J. Qi, J. Han, X. Zhou, D. Yang, J. Zhang, W. Qiao, D. Ma, Z. Y. Wang, *Macromolecules* **2015**, 48, 3941.

[38] G. Zhang, X.-K. Chen, J. Xiao, P. C. Y. Chow, M. Ren, G. Kupgan, X. Jiao, C. C. S. Chan, X. Du, R. Xia, Z. Chen, J. Yuan, Y. Zhang, S. Zhang, Y. Liu, Y. Zou, H. Yan, K. S. Wong, V. Coropceanu, N. Li, C. J. Brabec, J.-L. Brédas, H.-L. Yip, Y. Cao, *Nat Commun* **2020**, *11*, 3943.